RSC Advances

PAPER

View Article Online
View Journal | View Issue

Cite this: *RSC Adv.*, 2018, **8**, 2048

Hybrid BiOBr/UiO-66-NH_2 composite with enhanced visible-light driven photocatalytic activity toward RhB dye degradation†

Rehana Bibi,[a] Quanhao Shen,[a] Lingfei Wei,[a] Dandan Hao,[a] Naixu Li*[a] and Jiancheng Zhou *[abc]

Received 18th October 2017
Accepted 6th December 2017

DOI: 10.1039/c7ra11500h

rsc.li/rsc-advances

Metal–organic framework (MOFs) based composites have received more research interest for photocatalytic applications during recent years. In this work, a highly active, visible light photocatalyst BiOBr/UiO-66-NH_2 hybrid composite was successfully prepared by introducing various amounts of UiO-66-NH_2 with BiOBr through a co-precipitation method. The composites were applied for the photocatalytic degradation of RhB (rhodamine B) dye. The developed BiOBr/UiO-66-NH_2 composites exhibited higher photocatalytic activity than the pristine material. In RhB degradation experiments the hybrid composite with 15 wt% of UiO-66-NH_2 shows degradation efficiency conversion of 83% within two hours under visible light irradiation. The high photodegradation efficiency of BUN-15 could be ascribed to efficient interfacial charge transfer at the heterojunction and the synergistic effect between BiOBr/UiO-66-NH_2. In addition, an active species trapping experiment confirmed that photo-generated hole$^+$ and O_2^- radicals are the major species involved in RhB degradation under visible light.

1. Introduction

Water pollution caused by organic pollutants is one of the main environmental problems for human society. Among various techniques, such as physical, chemical, and biological degradation of organic pollutants in wastewater, photo-reduction through semiconductors is one of the promising strategies used to effectively degrade organic pollutants.[1] A lot of conventional semiconductors, named TiO_2,[2] ZnO,[3] and Cu_2O[4] have been widely studied for photocatalysis. However, they often restricted because of their lower absorptive properties for pollutants as well as low absorbance in the visible spectra range.[5–7] Metal–organic frameworks (MOFs), a new class of hybrid porous materials, get much research interest in last few years. Because of their attractive properties, such as designable framework architecture, tunable pore size, high specific surface areas, and the possibility of being functionalized,[8] it has been used in many fields like gas storage, separation, biomedicine, catalysis, and sensor devices. Recently research interest has been focused on their utilization as photocatalysts for organic pollutants removal.[9] Many MOFs, such as MOF-5,[10] MIL-53(Fe),[11] MIL-88(Fe),[12] and MIL-101(Fe)[13] could be excited under UV-visible-light due to their ligands to metal charge transfer.[14] However, compared to the inorganic semiconductor, the performance of MOFs is quite low because MOFs' are not enough efficient in solar energy conversion and separation of photogenerated charge transfer. Recently, incorporation of MOFs with light-harvesting semiconductor materials has been well known as an effective way for the production of the effective photocatalysts. Compared with MOFs themselves, the hybrid nanocomposite shows significant results due to their synergistic effect. For example, the micro core–shell structure of MIL-125(Ti) and In_2S_3 and its application as a photocatalyst for tetracycline's removal from water.[15] MIL-88(Fe) and MIL-53(Fe) were decorated by GO (graphene oxide) for the rhodamine B (RhB) degradation under visible light irradiation.[16,17] Ag/AgCl/MIL-101 hybrid composites were applied for the RhB degradation under visible-light.[18] In these examples, MOFs supported semiconductor composites shows better photocatalytic performance compared to the unsupported semiconductor materials. Therefore, MOFs are considered to be an ideal support for semiconductor materials for the photocatalytic applications in wastewater treatment. Amongst all of the MOF-based photocatalysts UiO-66-NH_2, a Zr-containing MOF composed of hexameric Zr_6O_{32} units linked by 2-aminoterephthalic acid (ATA) have been most widely investigated.[19–21] Though UiO-66-NH_2 has been used in a number of photocatalytic applications, but its performance is relatively low compared to other reported MOFs based photocatalysts, because of its inefficient charge transfer from the excited ligands (ATA) to

[a]School of Chemistry and Chemical Engineering, Southeast University, Nanjing, 211189, P. R. China. E-mail: jczhou@seu.edu.cn; naixuli@seu.edu.cn; Fax: +86 025 52090620; Tel: +86 025 52090621

[b]Department of Chemical and Pharmaceutical Engineering, Southeast University, Chengxian College, Nanjing, 210088, P. R. China

[c]Jiangsu Province Hi-Tech Key Laboratory for Biomedical Research, Southeast University, Nanjing 211189, PR China

† Electronic supplementary information (ESI) available: Pore size and surface area of BiOBr and UiO-66-NH_2, percentage degradation of RhB dye, SEM images of composites. See DOI: 10.1039/c7ra11500h

the Zr–O clusters, which is the most general photochemical process in MOF based nanocomposite.[22] Therefore, to find some strategies to improve the proficiency of the charge separation in UiO-66-NH_2 is appropriate for its use in photocatalysis. Several strategies, such as loading of noble metal nanoparticles and modifying of organic linkers have been developed for the improving of their photocatalytic activity.[23] Recently, Li *et al.* investigated that a partial substitution of Zr in NH_2-UiO-66 by Ti can improve the photocatalytic performance of this material for both CO_2 reduction and H_2 evolution.[24] On the other side, a number of reports are available in literature that focusing on bismuth oxyhalides (BiOX, X = Cl, Br, I) based photocatalysts, because of their high photocatalytic activity and comparatively convenient synthetic procedure.[25–28] Among all of these bismuth oxy-halides, BiOBr has many reports in the literature for photocatalytic degradation of organic dyes under visible light irradiations.[29,30] It has been found that photocatalytic activity can be enhanced by the combination of two different semiconductors *via* a synergistic effect, through which more efficient charge separation take place.[31,32] In the current work, BiOBr/UiO-66-NH_2 (named as BUN system) composites have successfully synthesized by Co-precipitation method for the enhancement of the photocatalytic activity of BiOBr flakes and UiO-66-NH_2 through a synergistic effect. The results showed that the BiOBr/UiO-66-NH_2 photocatalysts have greatly enhanced RhB photodegradation efficiency under visible light irradiation compared with pristine. Additionally, the probable photocatalytic mechanism for the RhB dye degradation over BiOBr/UiO-66-NH_2 is also discussed.

2. Experimental

2.1 Materials

Bismuth nitrate pentahydrate ($BiNO_3)_3\cdot 5H_2O$, zirconium chloride ($ZrCl_4$), sodium bromide (NaBr), and 2 amino-1,4-benzene dicarboxylic acid (H_2BDC-NH_2, $C_8H_7NO_4$ (99%)) were obtained from Alfa Aesar, China Co. *N*,*N*-Dimethylformamide [DMF], ethanol, and acetic acid were purchased from Sinopharm Chemical Reagent Co., Ltd. (Shanghai, China). All of the chemicals and solvents were of analytical grade and used without further purification.

2.2 Characterization

X-ray powder diffraction (XRD) patterns of the UiO-66-NH_2, BiOBr and BUN-*X* were recorded with a D8-Discover (Bruker, Germany) operating with Cu Kα radiation at 30 kV and 10 mA with a scanning angle (2θ) ranges from 5 to 80 at the scanning rate of 10 deg min^{-1}. The morphologies of the prepared samples were observed through a scanning electron microscope (SEM) model (EPMA-8705QH2, Shi-147 Shimadzu Co, Japan). Nitrogen adsorption–desorption isotherms were measured by a Micromeritics ASAP 2020 M system at liquid nitrogen temperature (77 K). The specific surface area (BET) was derived using the Brunauer, Emmett, and Teller (BET) method. The pore size distributions and the average pore diameter were measured using the BJH pore method. X-ray photoelectron spectroscopy (XPS) was conducted on a 2000 XPS system with a monochromatic Al-Kα source and a multichannel detector. Before the test, the calcined sample was reduced in H_2 at 250 °C for 2 h. The obtained binding energies were calibrated using the C 1s peak as a reference at 286.4 eV. The experimental error was given within $\pm$0.1 eV. Fourier transform infrared spectroscopy (FT-IR) was carried out with a Germany Bruker Company EQUI-NOX55 by means of KBr pellet technique with 163 scanning wavelength range of 4000–400 cm^{-1}. The actual amount of contents in the composites were evaluated by ICP-MS.

2.3 Synthesis of UiO-66-NH_2

UiO-66-NH_2 was prepared according to the reported protocol with slight modifications.[33] In a typical procedure, a mixture of $ZrCl_4$ (0.233 g, 1.0 mmol) and 2-amino-1,4-benzene dicarboxylic acid (0.1812 g, 1.0 mmol) was dissolved in 50 mL of DMF, then the solution was transferred to a 100 mL Teflon-lined stainless-steel autoclave. The autoclave was sealed and heated at 140 °C for 24 hours. After cooling to the room temperature, the product was obtained by centrifugation, washed by ethanol three times to remove DMF molecules, and dried under vacuum at 70 °C overnight.

2.4 Synthesis of BiOBr/UiO-66-NH_2 hybrid composites

Different MOF contents as 3, 7, 10, 15, 20, and 25 wt% named as BUN-3, BUN-7, BUN-10, BUN-15, BUN-20, and BUN-25, respectively were used for the preparation of hybrid composites. A specific amount of MOF was poured into 40 mL of water solution containing 0.24 g of NaBr under the process of ultrasonication furthermore, 0.97 g of $Bi(NO_3)\cdot 5H_2O$ was dissolved in 5 mL of acetic acid. By mixing the NaBr solution with acidic solution an off-white precipitate was formed immediately. After 30 minutes of magnetic stirring, the above mixture was transferred to a Teflon autoclave and heated at 110 °C for 8 hours. After cooling to the room temperature, the products were obtained by centrifuging, thoroughly washed with water and absolute ethanol to remove the ionic species, and dried at 70 °C overnight.

2.5 Evaluations of photocatalytic activity

Photocatalytic activity of the prepared composites was studied by the photodegradation of rhodamine (RhB) dye through visible light illumination in the photochemical reaction cell, equipped with a 500 W Xe lamp. Each experiment was run with 40 mg of the catalyst and 250 mL of 10 mg L^{-1} RhB dye. Before exposing to the visible light irradiation, the solution was ultrasonicated for 5 minutes followed by magnetic stirring for 30 minutes without light in order to achieve the adsorption equilibrium between the RhB molecules and catalyst. After exposing to the visible-light irradiation with continuous stirring, a 5 mL solution was collected, and filtered through a syringe filter (PTFE, hydrophobic 0.45 μm) to remove the product. The absorbance value of dye was measured at a 553 nm wavelength through UV-vis spectrophotometer (Perkin Elmer, Lambda 35).

2.6 Photoelectrochemical measurement

The photocurrent measurements were performed in a conventional three electrodes cell, containing a Pt plate as a counter

electrode, Ag/AgCl as a reference electrode, composites coated ITO plate as a working electrode and 0.3 M Na_2SO_4 aqueous solution as an electrolyte solution. The working electrode was prepared by mixing 8 mg of the prepared samples with 0.5 mL of PEDOT:PSS (solvent) along with 0.5 mL deionized water followed by grinding into a fine slurry. The above-prepared slurries were spread on pretreated ITO glass (0.5 cm × 1 cm) and dried in an oven at 60 °C for 30 minutes. A 500 W Ex. arc lamp with a 400 nm cut-off filter was invoked as the light source in the photo electrochemical measurements.

2.7 Photocatalytic mechanism investigation

In order to investigate the photocatalytic mechanism of the prepared photocatalyst, triethanolamine (TEOA), benzoquinone (BQ), and isopropyl alcohol (IPA) were added as a scavenger for ($hole^+$),[34] superoxide radical ($^{\bullet}O^{2-}$),[35] and hydroxyl radical ($^{\bullet}OH$)[36] to the RhB solution to give 1 mM concentration and keep all the other experimental conditions remain the same as given for photodegradation experiment.

3. Result and discussion

3.1 Morphology and composition of photocatalysts

The morphological structures of pristine and corresponding composite were studied with the help of X-ray powder diffraction (XRD) technique and the results are given in Fig. 1. XRD pattern for UiO-66-NH_2 (Fig. 1(a)) is in accordance with the literature, which shows a successful synthesis of MOF.[33] XRD diffractogram of BiOBr Fig. 1(b) shows number of diffraction peaks with well index (001), (002), (011), (012), (110), (020), (114), (212) crystal planes that support tetragonal phase for BiOBr. As per the hybrid composite XRD pattern all of the BiOBr peaks and the diffraction peak between 6 and 10 for UiO-66-NH_2 are observed, which indicate the existence of MOF and BiOBr in the composite, it also suggesting that MOF structure remain unchanged under the preparation process, a similar condition can also be found in other BiOBr/MOFs system.[37] However, some changes were observed in the crystals facets especially in (001) (012) and (110) crystal planes Fig. 1(b), which indicates that UiO-66-NH_2 might affect the BiOBr crystals growth that leads to different growing preference of the crystal facets. In order to determine the content of MOF in the prepared composite thermogravimetric analysis was carried out from 10 to 1000 °C in air (100 mL min^{-1} flow) atmosphere at a heating rate of 10 °C min^{-1} as shown in Fig. 1(c). Pure BiOBr shows a drastic weight loss from 600 °C to 700 °C owing to the degradation and formation of Bi_2O_3, while the TGA curve for UiO-66-NH_2 shows a progressive weight loss at 300 °C with a clear shoulder at 100 °C, which indicates the removal of physisorbed water as well as solvent molecules, while the weight loss from 300 to 500 °C shows the complete decomposition of MOF structure leads to the formation of ZrO_2.[38] In the TG study of BUN-15, the weight loss from 350 to 500 °C is due to the decomposition of UiO-66-NH_2, while the changes take place from 550 to 700 °C is due to decomposition of BiOBr. FTIR

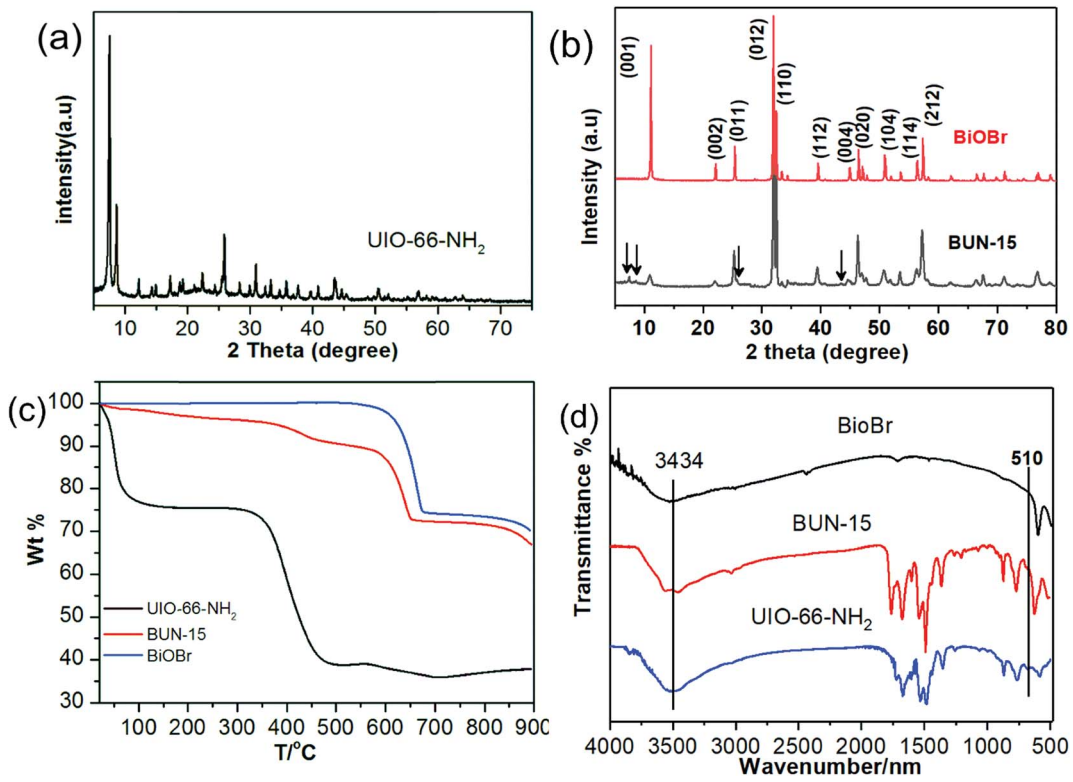

Fig. 1 (a) XRD pattern of UiO-66-NH_2, (b) XRD pattern BUN-15, (c) TGA spectra of BiOBr, UiO-66-NH_2, and BUN-15, and (d) FTIR spectra of BiOBr, UiO-66-NH_2, and BUN-15.

spectra of BiOBr, UiO-66-NH_2, and the BUN-15 composites are given in Fig. 1(d). In the BiOBr spectrum a sharp band at 510 cm^{-1} and a broad band at 3434 cm^{-1} are ascribed to the Bi–O stretching band, O–H stretching and O–H bending vibration of adsorbed water molecules.[40] The UiO-66-NH_2 spectrum consist of peaks from 600 to 800 are related to the Zr–O_2 longitudinal and transverse mode, while the peaks at 1429 and 1384 can be assigned to the carboxylic groups in the BDC-NH_2 ligands. The appearance of the absorption band at 1569.4 cm^{-1} indicates the reaction of –COOH with Zr^{4+} and the band at 1520.18 cm^{-1} is referred to the C=C from aromatic moiety.[16] Furthermore, all of the above MOF and BiOBr stretching modes could also be observed in the BUN-15 composite system with a slight shifting suggesting that the co-precipitation method completely retains the original structure and with the successful interaction of BiOBr and UiO-66-NH_2 Fig. 5(d).

The charge separation efficiency and prolong life time of photogenerated electrons–hole pairs were evaluated by PL (photoluminescence emission spectra). Fig. 2(a) show the PL spectra of pristine UiO-66-NH_2, BiOBr and BUN-15 with an excitation wavelength of 320 nm in the range of 400–600 nm wavelength. It can be observed that PL emission spectra of BUN-15 composite are lower than pristine BiOBr and UiO-66-NH_2 which shows that there is a low recombination of photogenerated electron–hole pairs. These results implied that BUN-15 has remarkably enhanced separation efficiency of photoinduced electron–hole pairs, which is well consistence with the results of transient photocurrent observations indicates that photogenerated electrons hole pairs are suppressed further when a heterojunction formed between MOF and BiOBr (Fig. 2(d)).[39] The UV-vis diffuse reflectance spectra (DRS) of the BUN-15 sample are shown in Fig. 2(b). The HOMO–LUMO energy band gap of BUN-15 can be estimated from the Tauc's plots using $\alpha(h\nu) = A(h\nu - E_g)^{n/2}$, where α, h, ν, E_g, and A are the absorption coefficient, Plank's constant, light frequency, band gap energy, and a constant, respectively. The coefficient 'n' is related to the optical transition of the semiconductors ($n = 1$ for direct transition and $n = 4$ for indirect transition). Based on the above equation, the band gap value (E_g) of BUN-15 was estimated as 2.76 eV. The estimated band gaps for pure BiOBr flakes and UiO-66-NH_2 are about 2.83 eV and 2.65 eV, respectively. The incorporation of specific amount of UiO-66-NH_2 with BiOBr decreases the catalyst band gap and improves the capability of the catalyst to get more visible light and give higher photocatalytic performance. The N_2 adsorption desorption isotherm of the BUN-15 are shown in Fig. 2(c). The surface area of the pure BiOBr and UiO-66-NH_2 were found to be 1.246 $m^2\ g^{-1}$ and 401 $m^2\ g^{-1}$, respectively, while that of BUN-15 was 30 $m^2\ g^{-1}$, which is greater than pristine BiOBr that may be favorable for the dye adsorption.

Fig. 3 represents the SEM images of UiO-66-NH_2, BiOBr, and BUN-*X*. It can be seen that UiO-66-NH_2 has an octahedral morphology with an average particle size of less than 200 nm (Fig. 3(a)). BiOBr exhibits nanosheets like structure with an average size of about 500–950 nm with diameter less than 50 nm Fig. 3(b). Pristine BiOBr retains their 2D lamella structure after

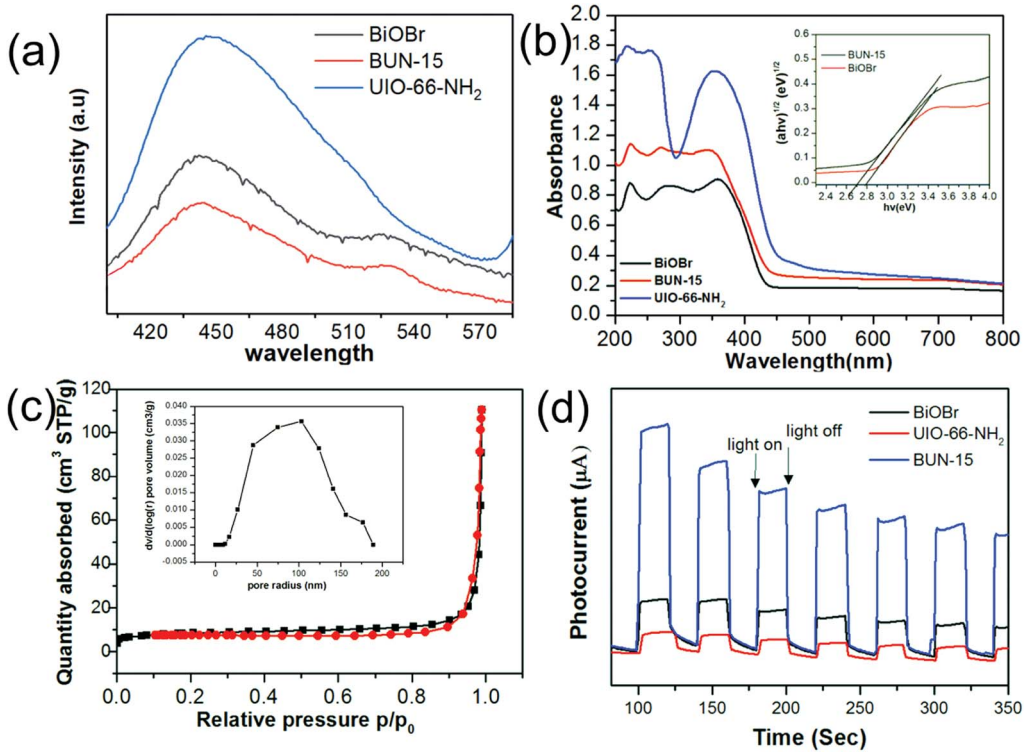

Fig. 2 (a) Photoluminescence spectra of prepared composites with an excitation wavelength of 320 nm, (b) UV-vis diffuse reflectance spectra of BUN-15, BiOBr, and UiO-66-NH_2; inset shows the optical absorption edges, and (c) N_2 adsorption–desorption BET surface area and BJH pore size of BUN-15 composite. (d) Transient photocurrent spectra of BiOBr, UiO-66-NH_2, BUN-15.

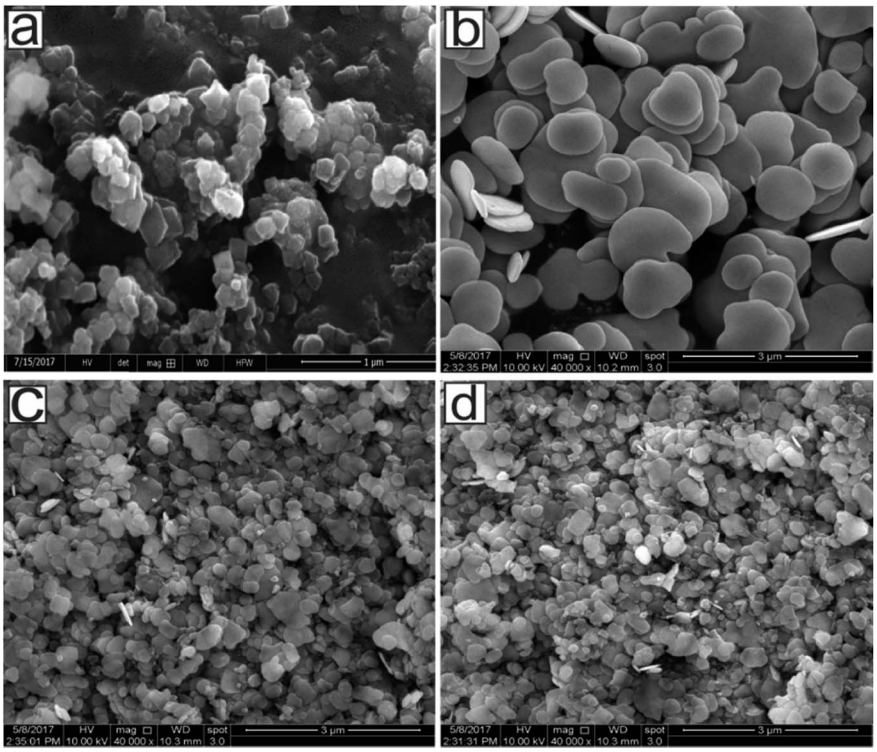

Fig. 3 (a) SEM images of UiO-66-NH_2, (b) BiOBr nanoflakes, (c) BUN-15, and (d) BUN-20.

incorporation of specific amount of UiO-66-NH_2. The surface composition and valence state of the elements were studied by X-ray photoelectron spectroscopy (XPS), As can be seen from Fig. (S1†) that the survey spectrum of BUN-15 shows the presence of Zr, Bi, Br, N, O, and C in the samples. As per Fig. 4(a), the observed peaks of BiOBr flakes at binding energies of 159.25 eV and 164.6 are attributed to Bi $4f_{7/2}$ and Bi $4f_{5/2}$, respectively, which are assigned to the Bi^{3+} in the composite.[40]

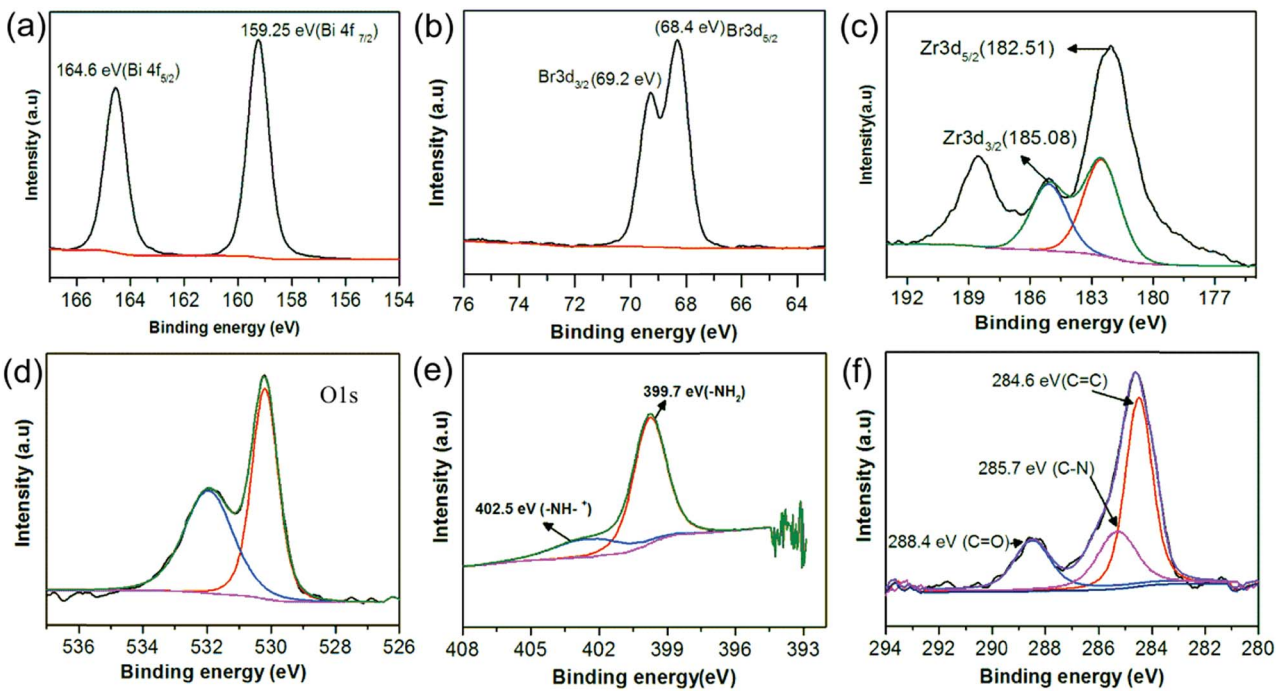

Fig. 4 XPS spectra of BUN-15 (a–f).

Peaks observed at 68.4 eV and 69.2 eV (Fig. 4(b)) are allocated to the Br $3d_{5/2}$, Br $3d_{3/2}$, respectively. The Zr 3d region can be deconvoluted into two peaks for Zr $3d_{5/2}$ and Zr $3d_{3/2}$ located at 182.5 eV and 185.0 eV (Fig. 4(c)), which are slightly shifted as compared to the original UiO-66-NH_2 peaks located at 182.84 eV and 185.17 eV, which suggest that BiOBr/UiO-66-NH_2 composites have been successfully synthesized.[41] The O 1s peak could be deconvoluted into two peaks located at 532.0 eV and 530.20 eV (Fig. 4(d)), which can be attributed to the carboxylate and other oxygen containing species.[42] C 1s peaks Fig. 4(e) are deconvoluted into three peaks located at 286.6 eV, 285.7 eV and 288.4 eV, which are assigned to the C–C, C–H (Sp^2) and C–N species and the carboxylate (O–C=O) group of ATA linkers, respectively.[43–45] Summarizing the above results, we can say that the enhanced photocatalytic activity of BUN-15 originates from the efficient interfacial charge transfer of the composite.

The morphology of these samples were also studied by TEM as shown in Fig. 5. It can be clearly observed from the TEM Fig. 5(c) that the MOF and BiOBr flakes are distributed uniformly without aggregation and well intercrossed with each other.

3.2 Photocatalytic activities of BiOBr, UiO-66-NH_2 and BUN-*X*

The photocatalytic activities of BiOBr, UiO-66-NH_2, and the prepared composites were evaluated by using the degradation of RhB under visible light irradiation. Self-photodegradation of dye are negligible as can be seen from (Fig. 6(a)) as the blank test. Owing to the poor charge separation efficiency of photogenerated electrons–holes pairs of MOF and small BET surface area of BiOBr, both UiO-66-NH_2 and BiOBr shows low photocatalytic activity before combining as shown in Fig. 6(a). However, the hybrid composites exhibit enhanced photocatalytic performance by degrading 83% of the RhB by BUN-15, 80% by BUN-20, and 81% by BUN-25 under visible light illumination for two hours of time (Fig. (S5†)), which is because of the combination of two semiconductors. Comparative UV-visible absorption spectra of RhB degradation over BUN-15 is shown in Fig. 6(b). One can see from Fig. 6(b) that the absorption peak value decreases with time and the results shows that the maximum absorption peak of RhB is blue-shifted, which is related with the de-ethylation process.[46] By comparing the results of BUN-*X* composites, BUN-15 shows higher photocatalytic activity for RhB degradation, which indicates the synergetic effect between BiOBr and UiO-66-NH_2. The kinetic curve over BUN-*X* photocatalysts for RhB degradation are plotted according to the pseudo-first-order kinetic model ($\ln C_0/C = kt$) and the *K* value are given in Fig. 6(d). The degradation rate order for the prepared photocatalysts is 0.01176 min^{-1} (BUN-15) > 0.00971 min^{-1} (BUN-25) > 0.0095 min^{-1} (BUN-20) > 0.00895 min^{-1} (BUN-10) > 0.00621 min^{-1} (BUN-7) > 0.00615 min^{-1} (BiOBr) > 0.00492 min^{-1} (BUN-3) > 0.000485 min^{-1} (UIO-66-NH_2) which are twenty-four times greater than MOF and two time greater than BiOBr. These results reveal that the Photocatalytic activity of BUN-*X* increases with the increase in the mass percent of UiO-66-NH_2 MOF from 3–15%. In addition, further increase in the MOF content causes a little decline in the photocatalytic activity as compared to the

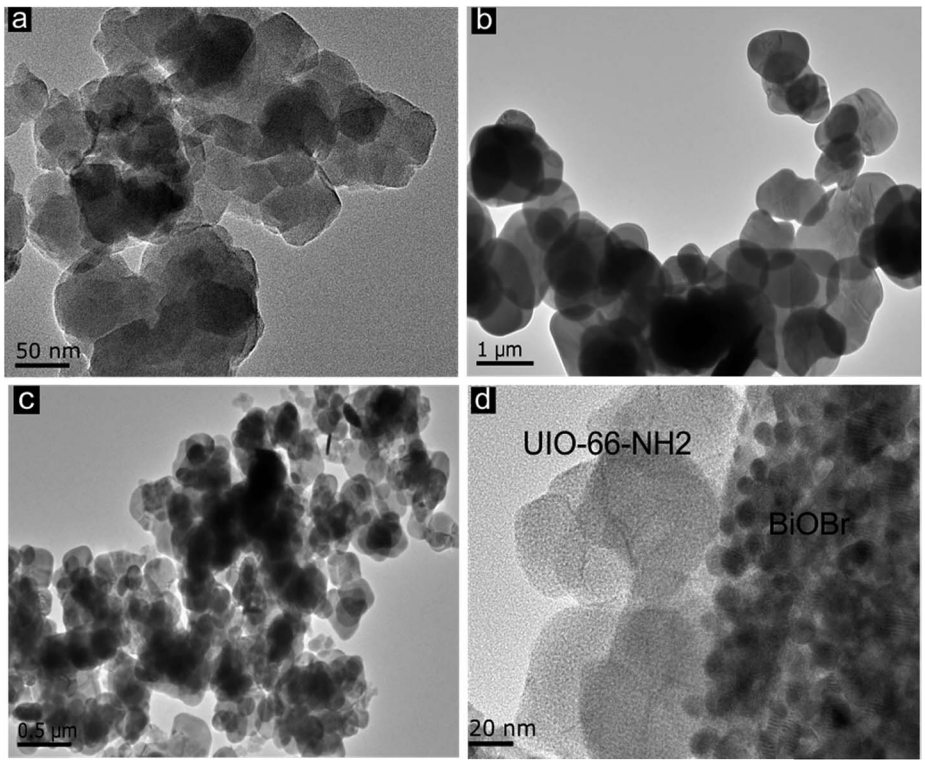

Fig. 5 TEM images of (a) UiO-66-NH_2, (b) BiOBr flakes, (c) BUN-15, and (d) HRTEM of BUN-15.

BUN-15, but still higher than pristine BiOBr and UiO-66-NH_2. This indicates that there is an optimum percentage value of content for the effective catalysts. Similarly, the little or more amount of UiO-66-NH_2 adversely affects the properties of the effective material in BUN-*X* composites, which is not suited for the material interfacial charge transfer.[47] In addition, to further reveal the contribution of the composite structure of BiOBr and UiO-66-NH_2 for dye degradation, a general experiment was carried out by the composites having an equal mass percent of BUN-15 through mechanically mixing method (Fig. 6(a) BUN-mix). The photocatalytic efficiency of BUN-15 was much greater than in physically mixed one, and an expected potential interaction has been formed between BiOBr and UiO-66-NH_2 which are more suitable for the transfer of photogenerated electron–hole pairs between them. Because of the random pattern between them, the accessible interspaces remains decreases. Thus, compared to the pure BiOBr, the BUN-15 composites have more accessible surfaces to interact with dye (RhB) molecules, which leads to an enhancement in the RhB degradation rate owing to the more transfer of electrons.[48]

3.3 Possible photodegradation mechanism of RhB dye

In order to explore the mechanism involved in photocatalytic degradation of RhB dye over BUN-15, the active species radical experiments were carried out by introducing TEOA as (holes$^+$ scavenger), IPA for $^{\bullet}OH$ radical, and BQ used for $^{\bullet}O_2^-$ radical scavenger, as shown in Fig. 6(c). It can be seen from the figure that with the addition of TEOA the degradation rate is significantly affected and decreases up to 30%, while with the addition of BQ the degradation decreases to 52%, which clearly indicates that the (h^+) and $^{\bullet}O_2^-$ radicals are the major species involved in the degradation of RhB dye. Similarly, no effect on the degradation process was observed with the IPA addition, which supports that $^{\bullet}OH$ radical has no role in the RhB degradation process.[41] Jiang *et al.* investigated the RhB degradation by photo catalytically generated (h^+) from BiOBr oxidation due to the dye adsorption on catalyst surface.[49] The flat-band potential of UiO-66-NH_2 was reported as (−0.60 V *vs.* NHE) which is more negative than the redox potential of O_2^- (0.28 V *vs.* NHE) and the calculated conduction band potential (CB is 2.15 *vs.* NHE).[50] The band edge position of BiOBr were evaluated by the empirical formula.[51]

$$E_{VB} = X - E^e + 0.5E_g \quad (1)$$

$$E_{CB} = E_{VB} - E_g \quad (2)$$

In which the *X* is the electronegativity of the semiconductor, the geometric mean of the absolute electronegativity of the constituent atom. E^e is the energy of free electron on hydrogen scale (0.45 V) and E_g is the band gap energy. The band edge potential VB of BiOBr were calculated as 3.11 and the CB edge potential were estimated to be 0.27 according to empirical formula (1) and (2). Based on the above discussion a schematic

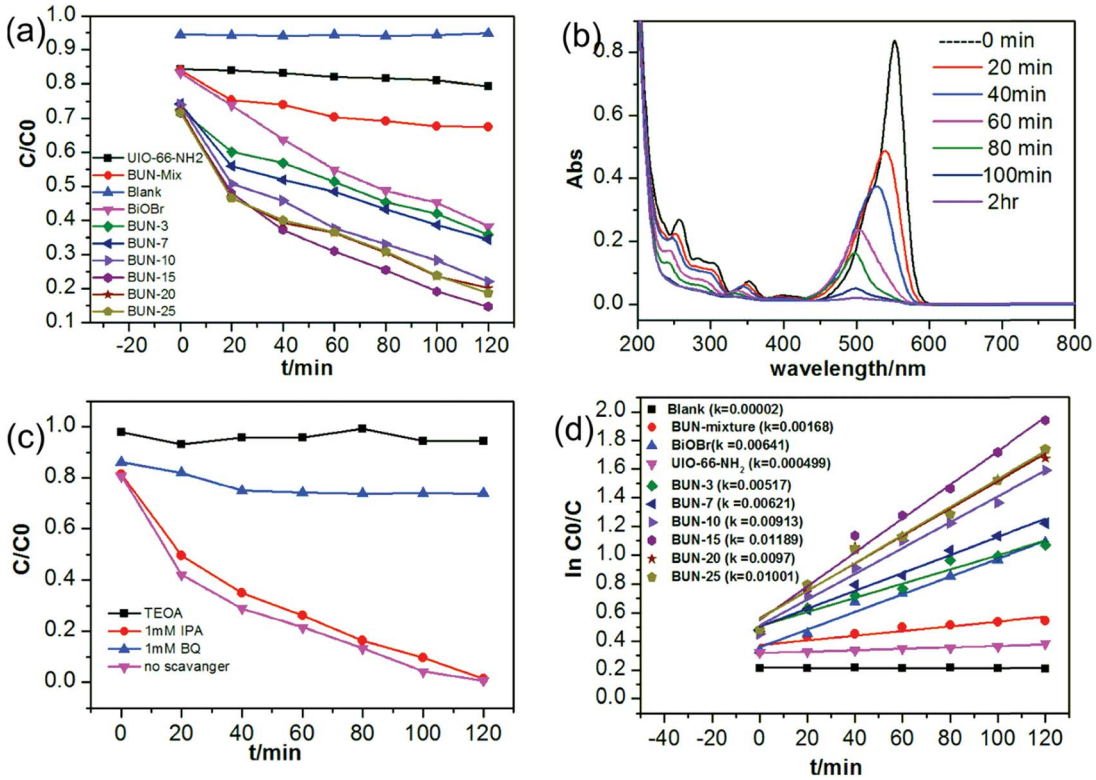

Fig. 6 (a) Photocatalytic degradation of RhB dye with different composites under visible light irradiation, (b) time-dependent UV-vis absorption spectra of BUN-15 (c) active species trapping experiments with BUN-15 under visible light irradiation, and (d) rate constant *k* comparison for different composites (pseudo-first-order kinetic model).

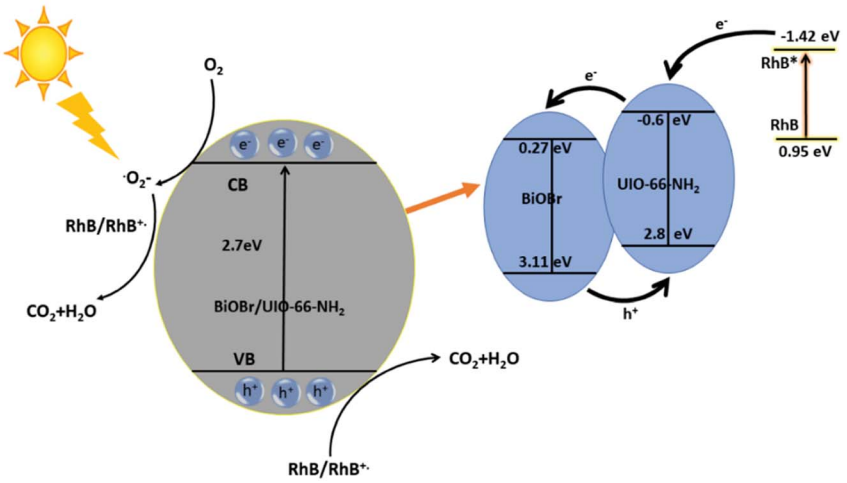

Scheme 1 Proposed mechanism of photocatalytic degradation of RhB dye by BUN-15 composite under visible light irradiation.

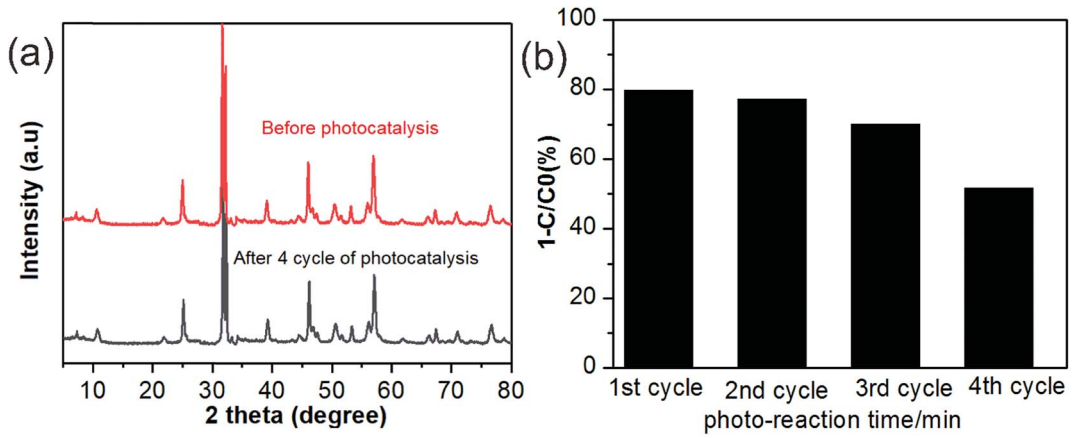

Fig. 7 (a) XRD pattern of BUN-15 before and after photo-degradation (b) reusability of BUN-15 for the photocatalytic degradation of RhB dye.

diagram of the formation of BiOBr/UiO-66-NH_2 and separation of photogenerated charge has been proposed in Scheme 1.

The CB potential edge of BiOBr is not enough negative to reduce O_2 to O_2- and further reduce RhB dye, so by considering the redox potential of RhB and excited RhB* are (0.95 V and −1.42 V *vs.* NHE) respectively. A reasonable explanation is that considering the potential of UiO-66-NH_2 (−0.60 V *vs.* NHE), direct electron transfer from RhB* to MOF is thermodynamically favorable then the electron could reduce the O_2 to O_2^- redial and further reduce the dye.[52] Once the BiOBr and UiO-66-NH_2 combine together the synergetic effect between the semiconductors can drive the migration of photogenerated and injected electron from UiO-66-NH_2 to BiOBr whereas the photogenerated holes transfer from BiOBr to MOF. The continuously transfer of electron and holes between the semiconductors increase the life time of charge carriers improving the efficiency of interfacial charge transfer. The photogenerated electrons can be captured by adsorbed O_2 to generate reactive O_2^- radicals, and then can breakdown the RhB dye. The photogenerated holes could serve as active sites for the photodegradation of organic contaminant.

Based on the above discussion, a plausible mechanism for the photocatalytic degradation of RhB dye by BUN-15 composite is presented in Scheme 1. In practical application the photocatalyst stability is very important, thus the stability of BUN-15 was also evaluated. After every photodegradation experiment, it was separated from the solution by a centrifuge, washed with methanol and water for many times, dried, and used again for the next cycle. Furthermore, the XRD test was also carried out after four cycles of photodegradation as given in Fig. 7(a) and the hybrid composites were found to be reused with enhanced photocatalytic activity. However, the photocatalytic efficiency of the catalyst decreased up to a certain extent with the reusing of time (Fig. 7(b)), which may be because of the adsorption of dye molecules in the pores of the catalyst surface.

4. Conclusion

A number of BiOBr/UiO-66-NH_2 hybrid composites with various amount of MOF were synthesized by co-precipitation method and applied for photocatalytic degradation of RhB dye. Most of the hybrid composites exhibited higher photocatalytic activity

for RhB dye, especially BUN-15 with the highest surface area (30 m^2 g^{-1}) and reactant kinetics (k = 0.01189 min^{-1}) than pristine UiO-66-NH_2 and BiOBr under visible light radiations. The enhanced photocatalytic activity can be described to the electron–hole pair's separation within the composite and synergistic effect between UiO-66-NH_2 and BiOBr with appropriate band gaps. Furthermore, the photogenerated hole (h^+) and $^{\bullet}O_2^-$ were found to be the major species involved in the dye degradation process. This work gives a good example that MOFs could be used as a capable substrate for photocatalytic activities in wastewater treatment. It may open up various opportunities for the development of further metal–organic framework based composites photocatalysts for organic pollutants removal in the future.

Conflicts of interest

There are no conflicts to declare.

Acknowledgements

This work was financially supported by the Fundamental Research Funds for the Central Universities of China (No. 3207045403, 3207045409, 3207046414), National Natural Science Foundation of China (No. 21576050 and No. 51602052), Jiangsu Provincial Natural Science Foundation of China (BK20150604), Priority Academic Program Development of Jiangsu Higher Education Institutions (PAPD), and Zhongying Young Scholars of Southeast University.

References

1 Z. Sha, H. S. O. Chan and J. Wu, Ag_2CO_3/UiO-66 (Zr) composite with enhanced visible-light promoted photocatalytic activity for dye degradation, *J. Hazard. Mater.*, 2015, **299**, 132–140.

2 E. Bailón-García, A. Elmouwahidi, M. A. Álvarez, F. Carrasco-Marín, A. F. Pérez-Cadenas and F. J. Maldonado-Hódar, New carbon xerogel-TiO_2 composites with high performance as visible-light photocatalysts for dye mineralization, *Appl. Catal., B*, 2017, **201**, 29–40.

3 X. Zhang, Y. Chen, S. Zhang and C. Qiu, High photocatalytic performance of high concentration Al-doped ZnO nanoparticles, *Sep. Purif. Technol.*, 2017, **172**, 236–241.

4 Q. Zhao, J. Wang, Z. Li, Y. Qiao, C. Jin and Y. Guo, Preparation of Cu_2O/exfoliated graphite composites with high visible light photocatalytic performance and stability, *Sep. Purif. Technol.*, 2016, **42**, 13273–13277.

5 H. Dong, G. Zeng, L. Tang, C. Fan, C. Zhang, X. He and Y. He, An overview on limitations of TiO_2-based particles for photocatalytic degradation of organic pollutants and the corresponding countermeasures, *Water Res.*, 2015, **79**, 128–146.

6 N. Muhd Julkapli, S. Bagheri and S. Bee Abd Hamid, Recent advances in heterogeneous photocatalytic decolorization of synthetic dyes, *Sci. World J.*, 2014, **2014**, 692307.

7 Y. Xia, J. Wang, R. Chen, D. Zhou and L. Xiang, A Review on the Fabrication of Hierarchical ZnO Nanostructures for Photocatalysis Application, *Crystals*, 2016, **6**, 148.

8 P. Deria, J. E. Mondloch, O. Karagiaridi, W. Bury, J. T. Hupp and O. K. Farha, Beyond post-synthesis modification: evolution of metal–organic frameworks via building block replacement, *Chem. Soc. Rev.*, 2014, **43**, 5896–5912.

9 C.-C. Wang, J.-R. Li, X.-L. Lv, Y.-Q. Zhang and G. Guo, Photocatalytic organic pollutants degradation in metal–organic frameworks, *Energy Environ. Sci.*, 2014, **7**, 2831–2867.

10 F. X. Llabrés i Xamena, A. Corma and H. Garcia, Applications for metal–organic frameworks (MOFs) as quantum dot semiconductors, *J. Phys. Chem. C*, 2007, **111**, 80–85.

11 R. Liang, F. Jing, L. Shen, N. Qin and L. Wu, MIL-53 (Fe) as a highly efficient bifunctional photocatalyst for the simultaneous reduction of Cr (VI) and oxidation of dyes, *J. Hazard. Mater.*, 2015, **287**, 364–372.

12 L. Shi, T. Wang, H. Zhang, K. Chang, X. Meng, H. Liu and J. Ye, An Amine-Functionalized Iron (III) Metal–Organic Framework as Efficient Visible-Light Photocatalyst for Cr (VI) Reduction, *Adv. Sci.*, 2015, **2**, 1500006.

13 D. Wang, R. Huang, W. Liu, D. Sun and Z. Li, Fe-based MOFs for photocatalytic CO_2 reduction: role of coordination unsaturated sites and dual excitation pathways, *ACS Catal.*, 2014, **4**, 4254–4260.

14 T. Tachikawa, J. R. Choi, M. Fujitsuka and T. Majima, Photoinduced charge-transfer processes on MOF-5 nanoparticles: elucidating differences between metal–organic frameworks and semiconductor metal oxides, *J. Phys. Chem. C*, 2008, **112**, 14090–14101.

15 H. Wang, X. Yuan, Y. Wu, G. Zeng, H. Dong, X. Chen, L. Leng, Z. Wu and L. Peng, In situ synthesis of In_2S_3@MIL-125 (Ti) core–shell microparticle for the removal of tetracycline from wastewater by integrated adsorption and visible-light-driven photocatalysis, *Appl. Catal., B*, 2016, **186**, 19–29.

16 Y. Wu, H. Luo and H. Wang, Synthesis of iron (III)-based metal–organic framework/graphene oxide composites with increased photocatalytic performance for dye degradation, *RSC Adv.*, 2014, **4**, 40435–40438.

17 C. L. Luu, T. T. Van Nguyen, T. Nguyen and T. C. Hoang, Synthesis, characterization and adsorption ability of UiO-66-NH2, *Adv. Nat. Sci.: Nanosci. Nanotechnol.*, 2015, **6**, 025004.

18 S. Gao, T. Feng, C. Feng, N. Shang and C. Wang, Novel visible-light-responsive Ag/AgCl@MIL-101 hybrid materials with synergistic photocatalytic activity, *J. Colloid Interface Sci.*, 2016, **466**, 284–290.

19 J. Long, S. Wang, Z. Ding, S. Wang, Y. Zhou, L. Huang and X. Wang, Amine-functionalized zirconium metal–organic framework as efficient visible-light photocatalyst for aerobic organic transformations, *Chem. Commun.*, 2012, **48**, 11656–11658.

20 L. Shen, R. Liang, M. Luo, F. Jing and L. Wu, Electronic effects of ligand substitution on metal–organic framework photocatalysts: the case study of UiO-66, *Phys. Chem. Chem. Phys.*, 2015, **17**, 117–121.

21 J. H. Cavka, S. Jakobsen, U. Olsbye, N. Guillou, C. Lamberti, S. Bordiga and K. P. Lillerud, A new zirconium inorganic building brick forming metal–organic frameworks with exceptional stability, *J. Am. Chem. Soc.*, 2008, **130**, 13850–13851.

22 M. A. Nasalevich, C. H. Hendon, J. G. Santaclara, K. Svane, B. Van Der Linden, S. L. Veber, M. V. Fedin, A. J. Houtepen, M. A. Van Der Veen and F. Kapteijn, Electronic origins of photocatalytic activity in d0 metal–organic frameworks, *Sci. Rep.*, 2016, **6**, 23676.

23 L. Shen, L. Huang, S. Liang, R. Liang, N. Qin and L. Wu, Electrostatically derived self-assembly of NH_2-mediated zirconium MOFs with graphene for photocatalytic reduction of Cr (vi), *RSC Adv.*, 2014, **4**, 2546–2549.

24 D. Sun, W. Liu, M. Qiu, Y. Zhang and Z. Li, Introduction of a mediator for enhancing photocatalytic performance via post-synthetic metal exchange in metal–organic frameworks (MOFs), *Chem. Commun.*, 2015, **51**, 2056–2059.

25 X. Chang, J. Huang, C. Cheng, Q. Sui, W. Sha, G. Ji, S. Deng and G. Yu, BiOX (X = Cl, Br, I) photocatalysts prepared using $NaBiO_3$ as the Bi source: characterization and catalytic performance, *Catal. Commun.*, 2010, **11**, 460–464.

26 H. Cheng, B. Huang and Y. Dai, Engineering BiOX (X = Cl, Br, I) nanostructures for highly efficient photocatalytic applications, *Nanoscale*, 2014, **6**, 2009–2026.

27 X. Zhang, Z. Ai, F. Jia and L. Zhang, Generalized one-pot synthesis, characterization, and photocatalytic activity of hierarchical BiOX (X = Cl, Br, I) nanoplate microspheres, *J. Phys. Chem. C*, 2008, **112**, 747–753.

28 L. Chen, R. Huang, M. Xiong, Q. Yuan, J. He, J. Jia, M.-Y. Yao, S.-L. Luo, C.-T. Au and S.-F. Yin, Room-Temperature Synthesis of Flower-Like BiOX (X = Cl, Br, I) Hierarchical Structures and Their Visible-Light Photocatalytic Activity, *Inorg. Chem.*, 2013, **52**, 11118–11125.

29 X.-X. Wei, C.-M. Chen, S.-Q. Guo, F. Guo, X.-M. Li, X.-X. Wang, H.-T. Cui, L.-F. Zhao and W. Li, Advanced visible-light-driven photocatalyst BiOBr–TiO_2–graphene composite with graphene as a nano-filler, *J. Mater. Chem. A*, 2014, **2**, 4667–4675.

30 H. Li, J. Liu, X. Liang, W. Hou and X. Tao, Enhanced visible light photocatalytic activity of bismuth oxybromide lamellas with decreasing lamella thicknesses, *J. Mater. Chem. A*, 2014, **2**, 8926–8932.

31 M. Zhou, J. Yu, S. Liu, P. Zhai and L. Jiang, Effects of calcination temperatures on photocatalytic activity of SnO_2/TiO_2 composite films prepared by an EPD method, *J. Hazard. Mater.*, 2008, **154**, 1141–1148.

32 M. Aramendía, V. Borau, J. Colmenares, A. Marinas, J. Marinas, J. Navío and F. Urbano, Modification of the photocatalytic activity of Pd/TiO_2 and Zn/TiO_2 systems through different oxidative and reductive calcination treatments, *Appl. Catal., B*, 2008, **80**, 88–97.

33 X. Hao, Z. Jin, H. Yang, G. Lu and Y. Bi, Peculiar synergetic effect of MoS_2 quantum dots and graphene on metal–organic frameworks for photocatalytic hydrogen evolution, *Appl. Catal., B*, 2017, **210**, 45–56.

34 Q. Li, X. Zhao, J. Yang, C.-J. Jia, Z. Jin and W. Fan, Exploring the effects of nanocrystal facet orientations in gC_3N_4/BiOCl heterostructures on photocatalytic performance, *Nanoscale*, 2015, **7**, 18971–18983.

35 M. Yin, Z. Li, J. Kou and Z. Zou, Mechanism investigation of visible light-induced degradation in a heterogeneous TiO_2/eosin Y/rhodamine B system, *Environ. Sci. Technol.*, 2009, **43**, 8361–8366.

36 L. Ye, J. Liu, Z. Jiang, T. Peng and L. Zan, Facets coupling of BiOBr-gC_3N_4 composite photocatalyst for enhanced visible-light-driven photocatalytic activity, *Appl. Catal., B*, 2013, **142**, 1–7.

37 Z. Sha and J. Wu, Enhanced visible-light photocatalytic performance of BiOBr/UiO-66 (Zr) composite for dye degradation with the assistance of UiO-66, *RSC Adv.*, 2015, **5**, 39592–39600.

38 L. Valenzano, B. Civalleri, S. Chavan, S. Bordiga, M. H. Nilsen, S. Jakobsen, K. P. Lillerud and C. Lamberti, Disclosing the complex structure of UiO-66 metal–organic framework: a synergic combination of experiment and theory, *Chem. Mater.*, 2011, **23**, 1700–1718.

39 S. Li, X. Wang, Y. Xu, H. Yang, F. Wei and X. Liu, The excellent photocatalytic synergism of $PbBiO_2$ Br/UiO-66-NH_2 composites via multiple coupling effects, *RSC Adv.*, 2016, **6**, 89907–89915.

40 J. Di, J. Xia, M. Ji, B. Wang, S. Yin, Q. Zhang, Z. Chen and H. Li, Advanced photocatalytic performance of graphene-like BN modified BiOBr flower-like materials for the removal of pollutants and mechanism insight, *Appl. Catal., B*, 2016, **183**, 254–262.

41 X.-F. Cao, L. Zhang, X.-T. Chen and Z.-L. Xue, Microwave-assisted solution-phase preparation of flower-like Bi_2WO_6 and its visible-light-driven photocatalytic properties, *CrystEngComm*, 2011, **13**, 306–311.

42 L. Shen, S. Liang, W. Wu, R. Liang and L. Wu, Multifunctional NH_2-mediated zirconium metal–organic framework as an efficient visible-light-driven photocatalyst for selective oxidation of alcohols and reduction of aqueous Cr (vi), *Dalton Trans.*, 2013, **42**, 13649–13657.

43 Y. Su, Z. Zhang, H. Liu and Y. Wang, $Cd_{0.2}Zn_{0.8}S$@UiO-66-NH_2 nanocomposites as efficient and stable visible-light-driven photocatalyst for H_2 evolution and CO_2 reduction, *Appl. Catal., B*, 2017, **200**, 448–457.

44 L. Shen, W. Wu, R. Liang, R. Lin and L. Wu, Highly dispersed palladium nanoparticles anchored on UiO-66 (NH_2) metal-organic framework as a reusable and dual functional visible-light-driven photocatalyst, *Nanoscale*, 2013, **5**, 9374–9382.

45 Y. Luan, Y. Qi, H. Gao, N. Zheng and G. Wang, Synthesis of an amino-functionalized metal–organic framework at a nanoscale level for gold nanoparticle deposition and catalysis, *J. Mater. Chem. A*, 2014, **2**, 20588–20596.

46 R. Wang, L. Gu, J. Zhou, X. Liu, F. Teng, C. Li, Y. Shen and Y. Yuan, Quasi-Polymeric Metal–Organic Framework UiO-66/g-C_3N_4 Heterojunctions for Enhanced Photocatalytic Hydrogen Evolution under Visible Light Irradiation, *Adv. Mater. Interfaces*, 2015, **2**(10), 1500037.

47 H. Wang, X. Yuan, Y. Wu, G. Zeng, X. Chen, L. Leng and H. Li, Synthesis and applications of novel graphitic carbon nitride/metal-organic frameworks mesoporous photocatalyst for dyes removal, *Appl. Catal., B*, 2015, **174**, 445–454.

48 S.-R. Zhu, M.-K. Wu, W.-N. Zhao, P.-F. Liu, F.-Y. Yi, G.-C. Li, K. Tao and L. Han, In Situ Growth of Metal–Organic Framework on BiOBr 2D Material with Excellent Photocatalytic Activity for Dye Degradation, *Cryst. Growth Des.*, 2017, **17**, 2309–2313.

49 Z. Jiang, F. Yang, G. Yang, L. Kong, M. O. Jones, T. Xiao and P. P. Edwards, The hydrothermal synthesis of BiOBr flakes for visible-light-responsive photocatalytic degradation of methyl orange, *J. Photochem. Photobiol., A*, 2010, **212**, 8–13.

50 L. Shen, S. Liang, W. Wu, R. Liang and L. Wu, CdS-decorated UiO-66 (NH_2) nanocomposites fabricated by a facile photodeposition process: an efficient and stable visible-light-driven photocatalyst for selective oxidation of alcohols, *J. Mater. Chem. A*, 2013, **1**, 11473–11482.

51 S.-R. Zhu, M.-K. Wu, W.-N. Zhao, F.-Y. Yi, K. Tao and L. Han, Fabrication of heterostructured $BiOBr/Bi_{24}O_{31}Br_{10}/TiO_2$ photocatalyst by pyrolysis of MOF composite for dye degradation, *J. Solid State Chem.*, 2017, **255**, 17–26.

52 J. He, J. Wang, Y. Chen, J. Zhang, D. Duan, Y. Wang and Z. Yan, A dye-sensitized Pt@UiO-66 (Zr) metal–organic framework for visible-light photocatalytic hydrogen production, *Chem. Commun.*, 2014, **50**, 7063–7066.